In vivo imaging of pyrrole-imidazole polyamides with positron emission tomography

Daniel A. Harki*, Nagichettiar Satyamurthy†, David B. Stout†, Michael E. Phelps†‡, and Peter B. Dervan*‡

*Division of Chemistry and Chemical Engineering, California Institute of Technology, Pasadena, CA 91125; and †Crump Institute for Molecular Imaging, Department of Molecular and Medical Pharmacology, David Geffen School of Medicine, University of California, Los Angeles, CA 90095

Contributed by Peter B. Dervan, June 30, 2008 (sent for review April 8, 2008)

The biodistribution profiles in mice of two pyrrole-imidazole polyamides were determined by PET. Pyrrole-imidazole polyamides are a class of small molecules that can be programmed to bind a broad repertoire of DNA sequences, disrupt transcription factor-DNA interfaces, and modulate gene expression pathways in cell culture experiments. The ^{18}F-radiolabeled polyamides were prepared by oxime ligation between 4-[^{18}F]-fluorobenzaldehyde and a hydroxylamine moiety at the polyamide C terminus. Small animal PET imaging of radiolabeled polyamides administered to mice revealed distinct differences in the biodistribution of a 5-ring β-linked polyamide versus an 8-ring hairpin, which exhibited better overall bioavailability. *In vivo* imaging of pyrrole-imidazole polyamides by PET is a minimum first step toward the translation of polyamide-based gene regulation from cell culture to small animal studies.

biodistribution | fluorine-18 | oxime | radiosynthesis

The development of chemical agents to regulate aberrant gene expression constitutes a promising strategy for treating human disease. These compounds function in cells by inhibiting the translation of mRNA gene products or by antagonizing transcription through direct DNA binding (1, 2). Pyrrole-imidazole polyamides are a class of cell permeable oligomers programmed to bind DNA sequence specifically with affinities similar to transcription factors (2–4). Encoded by pairs of aromatic amino acids *N*-methylpyrrole (Py) and *N*-methylimidazole (Im) (2), polyamides have been shown to target a wide range of discrete DNA sequences (5), localize to the nucleus in cell culture (6, 7), and access chromatin (8, 9). Polyamides can regulate endogenous gene expression through the disruption of DNA binding proteins in the promoters of selected genes. The binding of hypoxia-inducible factor (HIF-1α) to the hypoxia response element (HRE) has been antagonized by polyamides, resulting in the decreased expression of HIF-1α-regulated genes, including *VEGF* (10, 11). Androgen receptor (AR) binding to androgen response elements has also been inhibited by polyamides, yielding decreased expression levels of AR-regulated genes, such as *prostate-specific antigen* (12). A polyamide designed to inhibit activating protein-1 binding in the promoter of *TGF-β1* facilitated decreased levels of *TGF-β1* expression *in vitro* and *in vivo* (rats) (13). Gene activation has been achieved following polyamide treatment of a transcriptionally repressed cell culture model of Friedreich's ataxia (a trinucleotide repeat disease) (14). Given these promising biological activities in cell culture, tissue biodistribution studies of polyamides administered to animals is highly warranted. *In vivo* imaging of polyamides in discrete tissues would be of importance for the further development of polyamide-mediated gene regulation in animal models, a pivotal step toward clinical applications.

A new paradigm in early drug discovery has been the utilization of PET (15, 16). PET is an analytical imaging technology that measures real-time biodistribution of a positron-emitting probe administered to a subject. Through appropriate selection of the radiolabeled probe, a variety of biochemical processes relevant to human disease can be studied by PET (17, 18). Outside of the clinic, small animal PET is widely used in basic biomedical research and development, providing quantitative assays for the study of gene expression, metabolism and signal transduction, and drug biodistribution (15, 17–19). Preclinical drug screening by PET has been exploited for elucidating small molecule permeability to the blood-brain barrier (20, 21), and in human microdosing studies of experimental therapeutics during early clinical development (15, 16). In addition, the low-mass dose of radiolabeled PET probes (ie, high specific activity compounds injected at nanomolar concentrations, yielding picomoles of probe/g tissue) allows for detailed biodistribution analysis of target drugs without perturbing normal biological processes (17, 18).

In this study, we evaluated the real-time biodistribution of two polyamides of different classes, a 5-ring β-linked **1** (ImPyβImPyβImβ-C_3-^{18}F) and an 8-ring hairpin **3** [CtPyPyIm-$(R)^{H_2N}$γ-PyImPyPy-C_3-^{18}F], in mice with PET imaging [β, β-alanine; Ct, 3-chlorothiophene-2-carboxylic acid; $(R)^{H_2N}$γ, (*R*)-2,4-diaminobutyric acid]. Oxime ligation of radiolabeled 4-[^{18}F]-fluorobenzaldehyde (**6**) with hydroxylamine-functionalized **8** and **9** facilitated the rapid radiosynthesis of **1** and **3**. The DNA binding affinity of analogous ^{19}F-functionalized **2** and **4** was determined by quantitative DNase I footprinting, and the stability of the oxime linkage was evaluated *in vitro* and *in vivo*. PET/CT analysis of **1** and **3** in normal C57 mice revealed considerable liver uptake for both polyamides, with rapid gastrointestinal (GI) tract clearance for β-linked **1**. Interestingly, hairpin **3** exhibited substantially longer bioavailability, with minimal GI or renal clearance after 2 hours.

Results

Radiosynthesis. 4-[^{18}F]-fluorobenzaldehyde (**6**) was used as a radiochemical synthon (22–25) for the preparation of ^{18}F-labeled **1** and **3** (Fig. 1). Compound **6** was prepared by nucleophilic fluorination of trimethylammonium benzaldehyde derivative **5** at elevated temperature in the presence of the K^{18}F/Kryptofix [2.2.2] complex (Scheme 1) (25). Aniline accelerated oxime ligation (26) facilitated the conjugation of **6** to hydroxylamine-functionalized **8** and **9** in radiochemical yields of 12% (for **1**) and 7% (for **3**). Both syntheses were completed (material was HPLC purified) at ≈100 min after end of bombardment (EOB).

DNase I Footprinting. Quantitative DNase I footprint titrations were performed with ^{19}F-functionalized **2** and **4** to assess if the aminooxy-linked label **7** affects DNA binding. The binding affinity of **2** was measured on the 5′-^{32}P-PCR fragment from plasmid pJWP-17 (Fig. 2) (27). **2** bound the designed match site

Author Contributions: D.A.H., N.S., D.B.S., M.E.P., and P.B.D. designed research; D.A.H., N.S., and D.B.S. performed research; D.A.H., N.S., D.B.S., M.E.P., and P.B.D. analyzed data; and D.A.H., N.S., D.B.S., M.E.P., and P.B.D. wrote the paper.

The authors declare no conflict of interest.

‡To whom correspondence may be addressed. E-mail: dervan@caltech.edu or mphelps@mednet.ucla.edu.

This article contains supporting information online at www.pnas.org/cgi/content/full/0806308105/DCSupplemental.

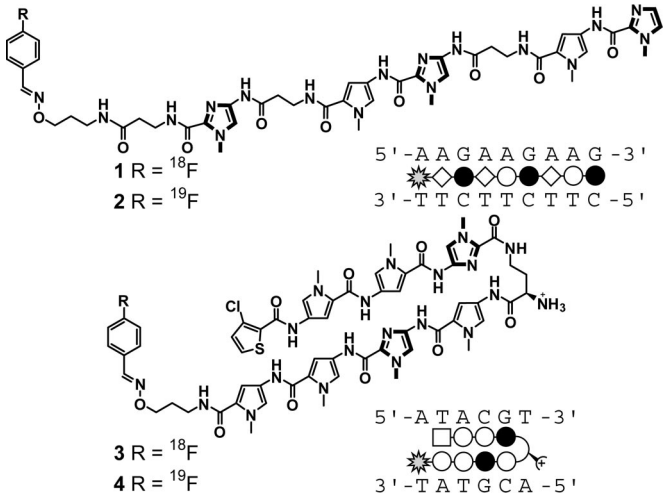

Fig. 1. Structures of **1** to **4** and their DNA binding sites. Closed circles designate *N*-methylimidazole, open circles designate *N*-methylpyrrole, diamonds represent β-alanine, and squares represent 3-chlorothiophene. The gray star designates the oxime-linked fluorine-18 or fluorine-19 label.

with $K_a = 3.5 \pm 2.1 \times 10^9\ M^{-1}$, which is ≈approximately sevenfold lower in binding affinity compared to the analogous polyamide possessing a *N*,*N*-dimethylaminopropyl tail (27). Hairpin **4** was studied on the 5′-^{32}P- PCR fragment from plasmid pGL2-VEGF-Luc (see Fig. 2) (10). Compound **4** bound the HRE match site with $K_a = 3.2 \pm 0.3 \times 10^9\ M^{-1}$. This binding affinity is ≈twofold and eightfold lower compared to polyamides of the same core sequence functionalized with an amide-linked 3,3′-diamino-*N*-methyldipropylamine tail terminated by either FITC (10) or an amide linked isophthalic acid moiety (28), respectively.

Evaluation of Oxime Stability. The pH stability of **4** was studied *in vitro* to evaluate the tolerance of the aminooxy linkage to acidic or basic cleavage. Solutions of **4** were incubated in pH 2.5, 4.0, 7.0, and 10 buffers at 37°C for 4 h, and then analyzed by ultra performance liquid chromatography-mass spectrometry (UPLC-MS). No significant degradation of **4** was observed at

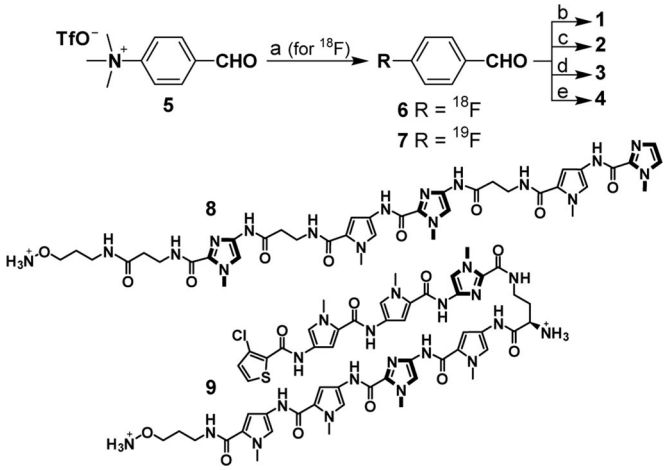

Scheme 1. Synthesis of **1**–**4**. (a) K^{18}F, Kryptofix [2.2.2], DMSO, 100°C, 10 min, 91% (decay-corrected). (b) **6**, **8**, TFA (aqueous), aniline, MeOH, 100°C (sealed tube), 20 min, 12% (decay-corrected). (c) **7**, **8**, NH_4OAc (aqueous), DMF, 40°C, 40 min, 49%. (d) **6**, **9**, NH_4OAc (aqueous), aniline, MeOH, 100°C (sealed tube), 20 min, 7% (decay-corrected). (e) **7**, **9**, NH_4OAc (aqueous), DMF, 40°C, 50 min, 41%.

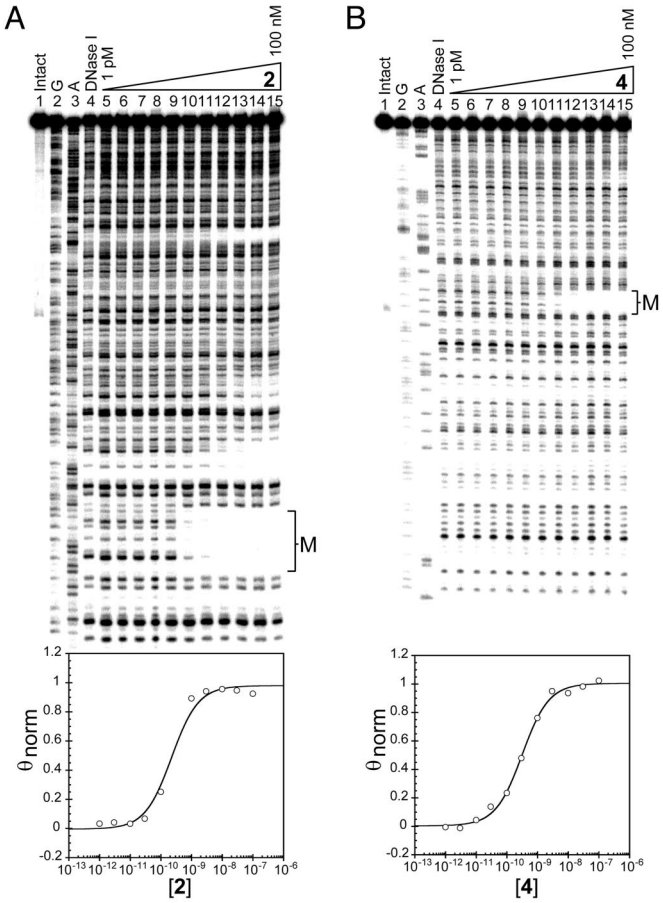

Fig. 2. Quantitative DNase I footprint titration experiments with **2** and **4**. Experiments were conducted on 5′-[^{32}P]-end-labeled PCR products of plasmid pJWP-17 (27) (for **2**) (*A*), or plasmid pGL2-VEGF-Luc (10) (for **4**) (*B*). The match binding sites are depicted on each gel (bracketed with M) and the corresponding binding isotherms are shown. Lanes 1 to 15 on each gel correspond to the following (in order): intact DNA, products of the G chemical sequencing reaction, products of the A chemical sequencing reaction, DNase I standard, 1 pM (polyamide treatment), 3 pM, 10 pM, 30 pM, 100 pM, 300 pM, 1 nM, 3 nM, 10 nM, 30 nM, 100 nM.

any pH examined [Fig. 3; MS data shown in supporting information (SI) Fig. S1]. To further probe the stability of this labeling strategy, 4-[^{18}F]-fluorobenzaldehyde (**6**) was administered to a normal C57 mouse and the biodistribution profile of **6** was measured by PET. As shown in Fig. S2, rapid kidney uptake of **6** was observed one minute after i.v. injection, with near exclusive bladder occupancy measured 30 min after treatment. This biodistribution profile differs dramatically from data obtained by PET imaging of **1** and **3** under identical conditions (Fig. 4).

Biodistribution. Radiolabeled **1** and **3** were administered intravenously to male C57 mice (dosages shown in Table S1) and tissue biodistribution was measured by PET/CT (Figs. 4 and 5). Both polyamides localized rapidly to the liver immediately upon injection, with **1** and **3** exhibiting (on average) 46% and 36% liver occupancy, respectively, ≈4 min after injection (see Fig. 5*A*). The 5-ring β-linked **1** was readily cleared from the liver by excretion through the gallbladder and entry into the small intestine, with 35 to 40% of the radioactive dose observed in the GI tract within the first 20 min. The 8-ring hairpin **3** exhibited constant levels of liver occupancy throughout the duration of the scan, and was excreted more slowly than **1** (eg, only 5% of the radioactive dose measured in the GI after 20 min). Elimination

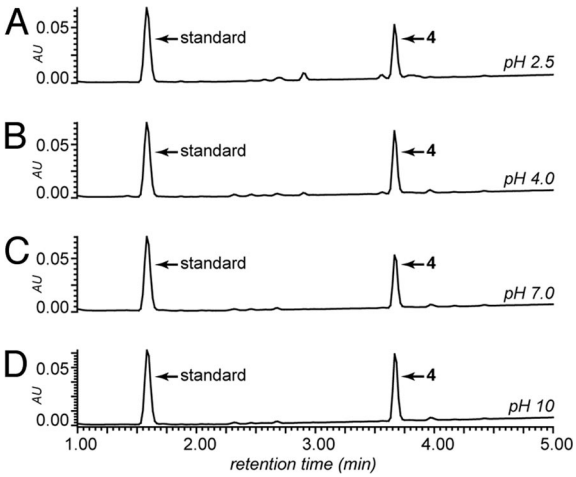

Fig. 3. pH stability analysis of **4**. **4** was incubated in pH 2.5 (*A*), pH 4.0 (*B*), pH 7.0 (*C*), and pH 10 (*D*) buffers at 37°C for 4 h. Samples were neutralized by addition of aqueous NH_4OAc containing 9-aminoacridine (standard), and then analyzed by UPLC-MS. DMI (1,3-dimethyl-2-imidazolidinone) (15%, vol/vol) was used as a cosolvent in the incubation and neutralization steps. Chromatograms shown (*A*–*D*) are UV detection at 254 nm. See Fig. S1 for MS data.

through the GI is favored over bladder excretion for both compounds. A constant level of **1** was observed in the gallbladder throughout the entire PET scan, whereas no significant levels of **3** were detected. Neither polyamide exhibited significant activity in the brain, heart, or bone.

Dosimetry. Biodistribution data obtained for **1** and **3** in mice were used to estimate the dosimetry values for a human model. The dose-limiting organ for **1** was the small intestine, with the urinary bladder wall, gallbladder, liver, and upper intestines possessing considerable radioactive doses (Table S2). For **3** the dose-limiting organ was the kidneys, with significant radioactive dose noted in the gallbladder, small intestine, liver, urinary bladder wall, and upper and lower intestines (Table S3).

Discussion

Recently, the use of PET in early drug development has gained considerable attention (15, 16). In this study, we assessed the tissue bioavailability and overall biodistribution of two ^{18}F-labeled polyamides of different classes (**1** and **3**) in mice using small animal PET.

The polyamide cores selected for biodistribution analysis in this study exhibit promising biological activities in cell culture.

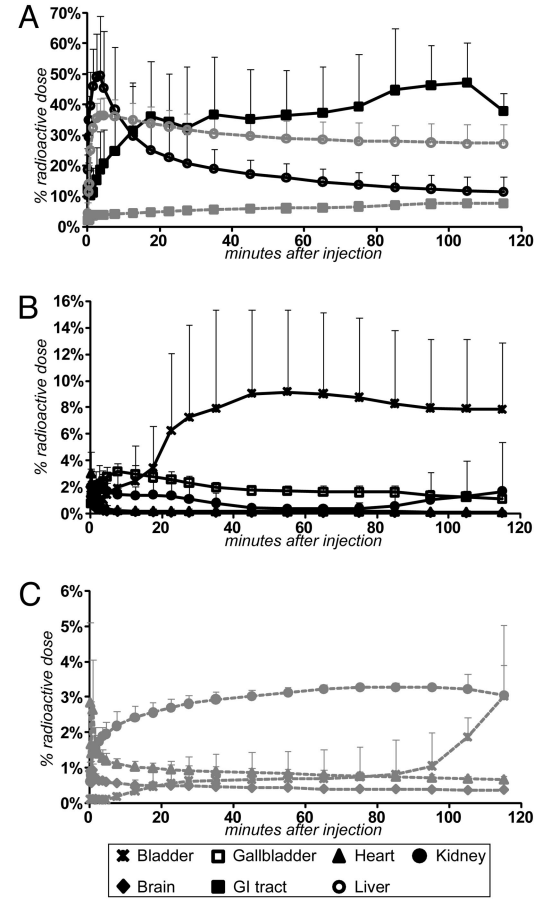

Fig. 5. Biodistribution of ^{18}F-labeled **1** (shown in *black*) and **3** (shown in *gray*) in mice by PET analysis. (*A*) Liver (open circles) versus GI (closed squares) occupancy for **1** and **3** over 2 h. (*B* and *C*) Remaining *in vivo* occupancy of **1** (*B*) and **3** (*C*) in mice, excluding the liver and GI values shown in *A*.

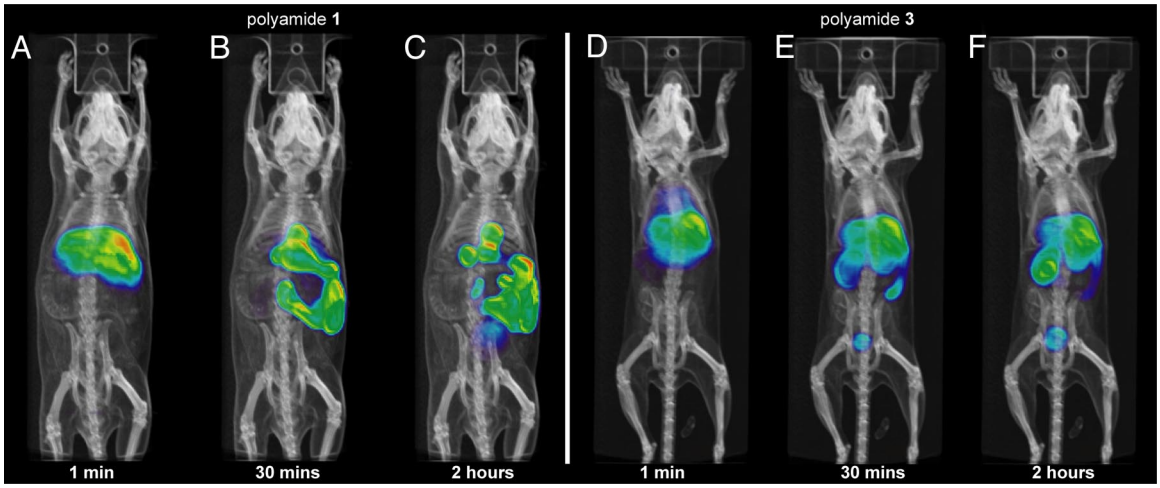

Fig. 4. PET/CT images of mice administered ^{18}F-labeled **1** (images *A*–*C*) and **3** (images *D*–*F*). Time-points shown are 1 min (*A* and *D*), 30 min (*B* and *E*), and 2 h (*C* and *F*) after injection.

The 5-ring β-linked polyamide (ie, the core of **1** with an *N*,*N*-dimethylaminopropyl tail) up-regulates expression of the repressed gene *frataxin* in a cell culture model of the disease Friedreich's ataxia (14). The 8-ring hairpin polyamide (ie, the core of **3**) downregulates hypoxia-induced *VEGF* expression in cell culture as either the FITC or isophthalic acid conjugate (10, 11, 28). Because the molecular recognition properties of polyamides are largely dictated by the arrangement of *N*-methylpyrrole and *N*-methylimidazole amino acids (2), we chose to append the polyamide C terminus (tail) with the ^{18}F-labeled prosthetic group to minimize its effects on DNA binding.

Although a variety of positron-emitting radioisotopes have been used for PET imaging, fluorine-18 is often considered the isotope of choice (29). Fluorine-18 possesses many favorable characteristics for PET imaging, including short positron range of travel in tissue, a suitable half-life (110 min), and a strong C–F bond with minimal perturbations to the native compound for monitoring a variety of biochemical processes *in vivo* (29, 30). For the radiosynthesis of polyamides described in this study, we used an oxime ligation between 4-[^{18}F]-fluorobenzaldehyde (**6**) and hydroxylamine-functionalized **8** and **9** to afford aminooxy-labeled **1** and **3**, respectively (see Scheme 1). This radiolabeling strategy has found widespread utility in the chemoselective radiolabeling of unprotected peptides for PET analysis (22–24), and offers significant advantages for the preparation of radiolabeled polyamides. For example, radiolabeled benzaldehyde **6** is readily synthesized by nucleophilic ^{18}F-fluorination of the triflate salt **5**, and easily purified on a solid-phase extraction cartridge (25, 31). This initial purification eliminates unreacted ^{18}F-fluoride ion carryover to the polyamide conjugation step. Additionally, the chemoselectivity of the oxime-forming reaction obviates the need to protect the chiral amine of **9**, thereby eliminating a deprotection step after radiolabeling. The recently described aniline-promoted transimination methodology for oxime synthesis was used in the radiosynthesis of **1** and **3** (26). **1** and **3** were prepared in overall radiochemical yields (decay-corrected) of 12% and 7%, respectively, at ≈100 min after EOB. The specific activity of **3** was measured to be >2,000 Ci/mmole at EOB, which demonstrates this methodology yields ^{18}F-labeled polyamides with high specific activities.

Quantitative DNase I footprint titrations were conducted to assess the DNA-binding penalty resulting from addition of the oxime-linked tag **6**. Fluorine-19 analogues **2** and **4** (see Fig. 1) were synthesized from commercially available **7** and evaluated on the 5′-^{32}P-PCR fragments from plasmid pJWP-17 (27) and pGL2-VEGF-Luc (10), respectively (see Fig. 2). β-linked **2** bound the designed match site with $K_a = 3.5 \pm 2.1 \times 10^9$ M^{-1} and hairpin **4** bound the HRE match site with $K_a = 3.2 \pm 0.3 \times 10^9$ M^{-1}. These binding affinities were only slightly lower (< 8-fold) than polyamides possessing the same cores but different functionalities on the tail (10, 27, 28). Therefore, the DNA binding penalty resulting from addition of the ^{18}F-radiolabel is minimal.

Although oxime conjugation of **6** to hydroxylamine-functionalized peptides has been reported previously for PET studies (22–24), we evaluated the pH tolerance of the oxime linkage *in vitro* and studied its stability *in vivo*. To probe pH stability, hairpin **4** was incubated in acidic (pH 2.5 and pH 4.0), neutral (pH 7.0) and basic (pH 10) solutions at 37°C for 4 h. Remarkably, no significant degradation of **4** was detected at any pH examined by UPLC-MS analysis (see Fig. 3). To assess *in vivo* stability of the ^{18}F-labeled polyamide, we also obtained PET/CT images of a mouse administered with 4-[^{18}F]-fluorobenzaldehyde (**6**). We rationalized that rapid hydrolysis of the oxime bond of **1** or **3** *in vivo* would liberate benzaldehyde **6** and yield similar biodistribution profiles for all compounds examined. PET imaging of a mouse injected with **6** revealed rapid kidney uptake of the tracer, followed by near exclusive bladder occupancy within 30 min (see Fig. S2). On the other hand, extremely low kidney and bladder uptake was observed for both polyamides in this study (see Fig. 5), and clearance through the GI tract was favored for both **1** and **3**. Therefore, oxime hydrolysis and the formation of 4-[^{18}F]-fluorobenzaldehyde (**6**) following injection seems quite unlikely.

The biodistribution profiles of a 5-ring β-linked **1** and an 8-ring hairpin **3** were evaluated by PET/CT imaging (see Figs. 4 and 5). For both polyamides rapid liver uptake was observed, with (on average) 46% (**1**) and 36% (**3**) of the injected radioactive dose localized in the liver ≈4 min after injection. A steady decrease in liver occupancy for β-linked **1** was paralleled by rapid entry into the gallbladder, followed by localization in the GI tract. Approximately ≈35 to 40% of **1** was observed in the GI tract within the first 20 min. This rapid clearance from the liver was not observed with hairpin **3**. After ≈20 min, only 5% of the injected dose of **3** was measured in the GI tract. The diminished pharmacokinetics of elimination for hairpin **3** suggests it possesses better overall bioavailability than β-linked **1**. Low levels of radioactivity were detected in the kidneys and bladder for both **1** and **3**, suggesting that excretion through the GI tract is the predominant method of elimination. Gallbladder occupancy remained constant throughout the duration of the scan for β-linked **1**, whereas no radioactivity was detected for hairpin **3**. Insignificant radiotracer levels were detected in the brain for both polyamides; therefore, neither **1** nor **3** crosses the blood-brain barrier. Activity was not detected in the heart or bone for either compound. Consequently, ^{18}F-labeled **1** and **3** are not defluorinated *in vivo* on the time scale of this experiment, as evidence by the absence of [^{18}F]-fluoride accumulation in bone.

The rapid elimination of **1** through the GI tract is reminiscent of the poor bioavailability of antisense phosphodiester oligonucleotides, another class of chemical agents used in gene regulation applications. Multiple biodistribution studies with radiolabeled (antisense) phosphodiester oligonucleotides have revealed significant renal clearance within the first hour following injection in baboons (32) and rats (33, 34). Similar results were also obtained in mice, with high radioactivity levels found in the kidney at the same time point (35). A recent PET study in mice treated with ^{64}Cu radiolabeled siRNA revealed similar clearance characteristics, with 23% of the injected dose measured in the liver and 73% of the injected dose delivered to the bladder after 1 h (36). Packaging of the radiolabeled siRNA complex into a nanoparticle did not significantly affect biodistribution. Compared with these studies and **1**, hairpin **3** is eliminated from the mouse less rapidly.

The tissue biodistribution of two structurally-related, DNA-binding small molecules, GSQ-2287 and Hoechst 33342, has been reported. GSQ-2287, a synthetic analogue of the natural product distamycin, localizes rapidly to the liver and kidney in mice shortly after injection (at therapeutic dose) and fails to cross the blood-brain barrier (37). Iodine-125 labeled Hoechst 33342 accumulates mostly in the kidneys (22% of injected dose), liver and spleen (≈7% of injected dose each) 4 h after injection (38). Aside from the kidney occupancies observed for both small molecules, the high liver values and failure to cross the blood-brain barrier is similar to data obtained for **1** and **3**.

Two biodistribution studies of hairpin polyamides administered to rodents have been reported previously. Dosage of a 10-ring (2-β-3 hairpin motif) fluorescein-labeled polyamide to rats (5 mg dose/250 g body weight) revealed considerable renal clearance at 24 h (13). This polyamide was also detected in the aorta, liver, and lung at the same time point, whereas no distribution to the heart or brain was observed. The liver uptake of **1** and **3** presented herein is consistent with this data, although 1 and 3 were both eliminated through the GI tract preferentially (see Fig. 5). It should be noted that GI tract occupancy was not evaluated in the aforementioned study (13). Recently, the phar-

macokinetics of a hairpin polyamide-chlorambucil conjugate dosed to mice (500 nmoles per mouse) was evaluated at two time-points (39). Predominant occupancy of the polyamide-alkylator conjugate was observed in the lung, spleen, small intestine, and pancreas at 2 and 24 h, as measured by liquid chromatography-mass spectrometry analysis (39). Elimination through the GI tract parallels the results obtained with **1** and **3** in this study. Interestingly, minimal liver occupancy was measured with the hairpin polyamide-alkylator conjugate at 2 h (39), whereas **3** is predominantly localized in the liver at the same time point.

Although both of the above-mentioned studies provide insights into polyamide bioavailability (13, 39), the necessity of animal killing and organ extraction permits only single time-point measurements to be conducted per animal. The methodology presented in this study permits examinations of polyamide biodistribution at multiple time points in the same animal, allowing detailed pharmacokinetic measurements to be performed in only a few hours. An example of the utility of this technology is shown in Fig. 5. As previously mentioned, hairpin **3** exhibits greater liver occupancy than β-linked **1** at 2 h. However, data obtained from PET imaging of **1** and **3** (see Fig. 5 *A*) reveals **1** to possess greater overall liver occupancy than hairpin **3** only minutes after injection. **1** is then rapidly cleared from the liver and distributed into the GI tract, whereas the level of hairpin **3** in the liver remains constant throughout the scan. The differences in the pharmacokinetics of elimination between **1** and **3** is readily observed by PET imaging, whereas classical, single time-point methods for studying compound biodistribution may fail to identify such subtle disparities.

PET imaging of ^{18}F-labeled **1** and **3** reveals distinct differences in tissue bioavailability between the two classes of polyamides, and constitutes the first bioavailability study of polyamides by this technology. In addition, a robust oxime-based radiolabeling procedure for the general preparation of ^{18}F-labeled polyamides has been described. These advances constitute a new tool for the further development of polyamide technology toward clinical applications, allowing candidate polyamides to be screened for favorable bioavailability properties during early chemical development.

Materials and Methods

Polyamide Synthesis. Protocols and Schemes S1–S4 for the synthesis of ^{18}F-labeled polyamides, fluorine-19 standards, and radiolabeling precursors can be found in the *SI Experimental Details*. Analytical HPLC characterization of ^{18}F-labeled compounds is shown in Fig. S3.

Determination of DNA Binding Affinities. Quantitative DNase I footprint titration experiments were conducted on 5′-^{32}P-PCR fragments from plasmid pJWP-17 (27) (2) and pGL2-VEGF-Luc (10) (4). Detailed experimental protocols have been reported previously (40).

pH Stability Analysis. Individual polyamide-buffer solutions were prepared by dissolving polymaride **4** (15 μl, 375 μM solution in DMI) in pH 2.5, 4.0, 7.0, or 10 buffers (85 μl, 20-mM high performance capillary electrophoresis grade buffers from Fluka) or distilled and deionized water (see Fig. S1). The polyamide solutions were shaken at 37°C for 4 h. Samples were neutralized by addition of a solution (100 μl) consisting of aqueous NH_4OAc (100 mM, pH 6.5; 85%, vol/vol), DMI (15%, vol/vol), and 9-aminoacridine (5.0 μM, Fluka) as internal standard for UPLC-MS analysis. Samples were vortexed, sonicated briefly (1 min), vortexed again, then immediately frozen in liquid nitrogen. Samples were stored at −80°C until analyzed. UPLC-MS analysis was performed on a Waters Acquity UPLC-LCT Premiere XE TOF-MS (ESI^+) system (see Fig. S1). A Waters Acquity UPLC BEH C18 column (2.1 × 50 mm, 1.7 μm) was used, with the mobile phase consisting of a gradient of MeCN (containing 0.1% formic acid) in formic acid (0.1%, aqueous). UV analysis was measured at 254 nm.

PET/CT Imaging. PET/CT imaging was conducted on male C57 mice under an approved protocol by the University of California at Los Angeles Animal Research Committee. Mice were kept warm, under 1 to 2% isoflurane gas anesthesia, and positioned using an imaging chamber. Fluorine-18-labeled **1** and **3** and control 4-[^{18}F]-fluorobenzaldehyde (**6**) were injected into the tail vein (dosages shown in Table S1). Data were acquired using a Siemens Preclinical Solutions microPET Focus 220 and microCAT II CT systems. PET data were acquired for 2 or 3 h and reconstructed using filtered back projection into 22 or 28 frames, respectively. PET images are ≈1.8-mm resolution, 0.4-mm voxel size. CT images are a low dose 400-μm resolution acquisition with 200-μm voxel size. Images were coregistered and regions drawn using AMIDE software (Andreas Loening, amide.sourceforge.net, Version 0.8.16).

Calculation of Biodistribution Values. The biodistribution graphs contain the percentage of total dose in each organ over 2 h. Liver values are based on a region drawn away from the gallbladder, with the mean value multiplied by the estimated weight derived from 4.5% of the mouse body weight (value from The Jackson Laboratory Web site). Kidney, heart and brain totals are from regions drawn on the PET images, and verified using the weights based on literature values as percent body weight (assuming density equals 1, thus volume equals weight). GI (1.75 g) and gallbladder (20 mg) weights are based on literature search estimated organ weights for a 25-g mouse.

Calculation of Dosimetry Values. The total number of disintegrations was calculated for each organ and the total body. The data were then extended to 7.5 h after injection to estimate the majority of the total number of disintegrations (≈4 half-lives for physical decay, accounting for >95% of all disintegrations). No bladder voiding or bowel movements were assumed. Using the residency time equivalent measure, dosimetry was calculated using OLINDA software (Version 1.0, Vanderbilt University, 2003). The adult male human model was used.

OLINDA is not designed for using PET data in mice to make human predictions. There are no S table values for the small organ sizes and distances in mice, so these data are preliminary and only provide a guide for estimating limiting dosage for potential human use and should be followed with human dosimetry to determine the proper dose limitations.

ACKNOWLEDGMENTS. We thank the staffs of the Biomedical Cyclotron Facility and the Crump Preclinical Imaging Center at the University of California, Los Angeles for helpful discussions and support, and Dr. Mona Shahgholi (California Institute of Technology) for assistance with UPLC-MS analysis. This work was supported by National Institutes of Health Grants GM27681, R01-EB001943, and R24 CA 92865; National Science Foundation Chemistry Research Instrumentation and Facilities Program Grant CHE-0541745; and the Department of Energy Cooperative Agreement DE-FC03-02ER63420. D.A.H. thanks the Friedreich's Ataxia Research Alliance and the California Tobacco-Related Disease Research Program (16FT-0055) for postdoctoral fellowships.

1. Hannon GJ, Rossi JJ (2004) Unlocking the potential of the human genome with RNA interference. *Nature* 431:371–378.
2. Dervan PB, Edelson BS (2003) Recognition of the DNA minor groove by pyrrole-imidazole polyamides. *Curr Opin Struct Biol* 13:284–299.
3. Trauger JW, Baird EE, Dervan PB (1996) Recognition of DNA by designed ligands at subnanomolar concentrations. *Nature* 382:559–561.
4. Dervan PB (2001) Molecular recognition of DNA by small molecules. *Bioorg Med Chem* 9:2215–2235.
5. Hsu CF, *et al.* (2007) Completion of a programmable DNA-binding small molecule library. *Tetrahedron* 63:6146–6151.
6. Best TP, Edelson BS, Nickols NG, Dervan PB (2003) Nuclear localization of pyrrole-imidazole polyamide-fluorescein conjugates in cell culture. *Proc Natl Acad Sci USA* 100:12063–12068.
7. Edelson BS, *et al.* (2004) Influence of structural variation on nuclear localization of DNA-binding polyamide-fluorophore conjugates. *Nucleic Acids Res* 32:2802–2818.
8. Edayathumangalam RS, Weyermann P, Gottesfeld JM, Dervan PB, Luger K (2004) Molecular recognition of the nucleosomal "supergroove." *Proc Natl Acad Sci USA* 101:6864–6869.
9. Dudouet B, *et al.* (2003) Accessibility of nuclear chromatin by DNA binding polyamides. *Chem Biol* 10:859–867.
10. Olenyuk BZ, *et al.* (2004) Inhibition of vascular endothelial growth factor with a sequence-specific hypoxia response element antagonist. *Proc Natl Acad Sci USA* 101:16768–16773.
11. Nickols NG, Jacobs CS, Farkas ME, Dervan PB (2007) Modulating hypoxia-inducible transcription by disrupting the HIF-1-DNA interface. *ACS Chem Biol* 2:561–571.
12. Nickols NG, Dervan PB (2007) Suppression of androgen receptor-mediated gene expression by a sequence-specific DNA-binding polyamide. *Proc Natl Acad Sci USA* 104:10418–10423.
13. Matsuda H, *et al.* (2006) Development of gene silencing pyrrole-imidazole polyamide targeting the TGF-beta1 promoter for treatment of progressive renal diseases. *J Am Soc Nephrol* 17:422–432.

14. Burnett R, *et al.* (2006) DNA sequence-specific polyamides alleviate transcription inhibition associated with long GAA•TTC repeats in Friedreich's ataxia. *Proc Natl Acad Sci USA* 103:11497–11502.
15. Bergström M, Grahnén A, Långström B (2003) Positron emission tomography microdosing: a new concept with application in tracer and early clinical drug development. *Eur J Clin Pharmacol* 59:357–366.
16. Weber WA, Czernin J, Phelps ME, Herschman HR (2008) Technology insight: novel imaging of molecular targets is an emerging area crucial to the development of targeted drugs. *Nat Clin Pract Oncol* 5:44–54.
17. Phelps ME (2000) Positron emission tomography provides molecular imaging of biological processes. *Proc Natl Acad Sci USA* 97:9226–9233.
18. Phelps ME (2000) PET: The merging of biology and imaging into molecular imaging. *J Nucl Med* 41:661–681.
19. Phelps ME (2002) Molecular imaging with positron emission tomography. *Annu Rev Nucl Part Sci* 52:303–338.
20. Lee CM, Farde L (2006) Using positron emission tomography to facilitate CNS drug development. *Trends Pharmacol Sci* 27:310–316.
21. Burns HD, *et al.* (1999) Positron emission tomography neuroreceptor imaging as a tool in drug discovery, research and development. *Curr Opin Chem Biol* 3:388–394.
22. Poethko T, *et al.* (2004) Two-step methodology for high-yield routine radiohalogenation of peptides: ^{18}F-labeled RGD and octreotide analogs. *J Nucl Med* 45:892–902.
23. Poethko T, *et al.* (2004) Chemoselective pre-conjugate radiohalogenation of unprotected mono- and multimeric peptides via oxime formation. *Radiochim Acta* 92:317–327.
24. Schottelius M, *et al.* (2004) First ^{18}F-labeled tracer suitable for routine clinical imaging of sst receptor-expressing tumors using positron emission tomography. *Clin. Cancer Res* 10:3593–3606.
25. Toyokuni T, *et al.* (2003) Synthesis of a new heterobifunctional linker, N-[4-(aminooxy)butyl]maleimide, for facile access to a thiol-reactive ^{18}F-labeling agent. *Bioconjugate Chem* 14:1253–1259.
26. Dirksen A, Hackeng TM, Dawson PE (2006) Nucleophilic catalysis of oxime ligation. *Angew Chem Int Ed* 45:7581–7584.
27. Puckett JW, *et al.* (2007) Quantitative microarray profiling of DNA-binding molecules. *J Am Chem Soc* 129:12310–12319.
28. Nickols NG, Jacobs CS, Farkas ME, Dervan PB (2007) Improved nuclear localization of DNA-binding polyamides. *Nucleic Acids Res* 35:363–370.
29. Lasne M-C, *et al.* (2002) Chemistry of beta+-emitting compounds based on fluorine-18. *Top Curr Chem* 222:203–258.
30. Wester HJ (2003) in *Handbook of Nuclear Chemistry*, eds Vertés A, Nagy S, Klenesár Z (Kluwer Academic Publishers, The Netherlands). pp 167–208
31. Wilson AA, Dannals RF, Ravert HT, Wagner HN, Jr. (1990) Reductive amination of [^{18}F]fluorobenzaldehydes: Radiosynthesis of [2-^{18}F]- and [4-^{18}F]fluorodexetimides. *J Labelled Compd Radiopharm* 28:1189–1199.
32. Tavitian B, *et al.* (1998) In vivo imaging of oligonucleotides with positron emission tomography. *Nat Med* 4:467–471.
33. Roivainen A, *et al.* (2004) ^{68}Ga-labeled oligonucleotides for in vivo imaging with PET. *J Nucl Med* 45:347–355.
34. Lendvai G, *et al.* (2005) Biodistribution of ^{68}Ga-labelled phosphodiester, phosphorothioate, and 2′-O-methyl phosphodiester oligonucleotides in normal rats. *Eur J Pharm Sci* 26:26–38.
35. Kühnast B, *et al.* (2000) General method to label antisense oligonucleotides with radioactive halogens for pharmacological and imaging studies. *Bioconjugate Chem* 11:627–636.
36. Bartlett DW, Su H, Hildebrandt IJ, Weber WA, Davis ME (2007) Impact of tumor-specific targeting on the biodistribution and efficacy of siRNA nanoparticles measured by multimodality in vivo imaging. *Proc Natl Acad Sci USA* 104:15549–15554.
37. Gross M, *et al.* (2003) Pharmacology of novel heteroaromatic polycycle antibacterials. *Antimicrob Agents Chemother* 47:3448–3457.
38. Harapanhalli RS, *et al.* (1996) [^{125}I/^{127}I]IodoHoechst 33342: Synthesis, DNA binding, and biodistribution. *J Med Chem* 39:4804–4809.
39. Chou CJ, *et al.* (2008) Small molecules targeting histone H4 as potential therapeutics for chronic myelogenous leukemia. *Mol Cancer Ther* 7:769–778.
40. Trauger JW, Dervan PB (2001) Footprinting methods for analysis of pyrrole-imidazole polyamide/DNA complexes. *Methods Enzymol* 340:450–466.